Chapter 5
Descriptions of Dislocation via First Principles Calculations

Tomohito Tsuru

5.1 Introduction

Dislocation, a line defect in which atoms are out of the lattice position in the crystal structure, is one of the most representative "plastons". A mathematical description of the elastic field of the singularity created by cutting and shifting a continuous body was first developed by Volterra in 1907 (Volterra 1907). Since Taylor, Orowan, and Polanyi predicted the existence of dislocation to explain plastic deformation (Taylor 1934; Orowan 1934; Polanyi 1934), dislocations have been regarded as the most important lattice defects in plastic deformation, especially in metallic materials. The fundamental properties of the dislocation core have a dominant influence on the intrinsic ductility or brittleness of materials. The interaction between dislocations and other crystal defects plays a critical role in determining the mechanical properties of metals. The classical strengthening mechanism was developed by this major premise, and the mechanical properties of metals have been developed by understanding and controlling the dislocation behavior.

While continuum theory expresses an excellently long-ranged elastic field of a dislocation, it breaks down owing to the singularity near the dislocation core. With improvements in computer technology, atomic scale simulations such as molecular dynamics have been implemented to explore the relation between the dynamic

In this Chapter, DFT calculations were carried out using the Vienna ab initio simulation package (VASP) (Kresse and Hafner 1993; Kresse and Furthmuller 1996) with the Perdew–Burke–Ernzerhof generalized gradient approximation exchange–correlation density functional (Perdew et al. 1992). The Brillouin-zone k-point samplings were chosen using the Monkhorst–Pack algorithm (Monkhorst and Pack 1976). The planewave energy cutoff was set at 400 eV. The fully relaxed configurations were obtained by the conjugate gradient method when the energy norm of all the atoms converged to better than 0.005 eV/Å. Simulations were performed on the large-scale parallel computer system with SGI ICE X at JAEA.

T. Tsuru (✉)
Nuclear Science and Engineering Center, Japan Atomic Energy Agency, Tokai, Ibaraki, Japan
e-mail: tsuru.tomohito@jaea.go.jp

I. Tanaka et al. (eds.), *The Plaston Concept*,
https://doi.org/10.1007/978-981-16-7715-1_5

behavior of defects and the mechanical response. Some examples of atomistic simulations for collective defect behavior were mentioned in the previous section. Recently, a dislocation core structure can be captured directly by first principles calculations. Several approaches for first principles calculations of dislocations and dislocation-related properties are described in detail in this section.

5.2 Stacking Fault Energy

The atomic image of a dislocation core is described by local disregistry, where misfit energy is introduced by the local interfacial misfit energy as well as the elastic strain energy. The misfit energy $\gamma(\mathbf{u})$ is described by periodic potential in terms of relative slip displacement, which is expressed by its sinusoidal shape potential in the classical model. Atomistic simulation, such as molecular dynamics and first principles, allows calculation of the misfit potential directly. Precise calculations of stacking fault (SF) energy can help to better understanding slip behavior in actual materials. The generalized SF energy (γ surface), which was first introduced by Vítek (Vítek 1966, 1968), is the energy difference in misfit energy in terms of two-dimensional displacement along the slip plane. Atomic models for SF energy in FCC metals are simply prepared as in Fig. 5.1, where parallel translation is applied to the upper half region. The energy of the transition during slip motion is evaluated using first principles calculations. The atomic relaxation is considered only in the normal direction to the slip plane and the other degree of freedom corresponding to the direction of the applied displacement is constrained. The difference in terms of displacement corresponds to the generalized SF energy according to following relation, where A is the area of the slip plane.

$$\gamma(\mathbf{u}) = \frac{E(\mathbf{u}) - E_0}{A}, \tag{5.1}$$

In FCC metals, the displacement is generally applied along the $[1\bar{1}0]$ and $[11\bar{2}]$ the directions defined as x and y. The Burgers vector of perfect dislocation corresponds to $a/2[1\bar{1}0]$, along which the SF energy is not minimum. Instead, the SF energy along the Burgers vector of partial dislocations is equivalent to the minimum energy path for parallel shift in the slip plane, which is important for actual slip behavior in FCC metals.

The SF energy curves for typical FCC and BCC metals calculated by first principles calculations are summarized in Fig. 5.2. The other results obtained by several empirical potential and experiments are shown as a comparison. γ_{SF} corresponds to the energy when the displacement is equivalent to the partial dislocation, shown in the right image in Fig. 5.1. The value is important in determining the stable dislocation core structure and the width between leading and trailing partial dislocations in FCC metals. Unstable SF energy γ_{us} and the maximum gradient of the generalized SF energy are also important because the local atomic array needs to overcome

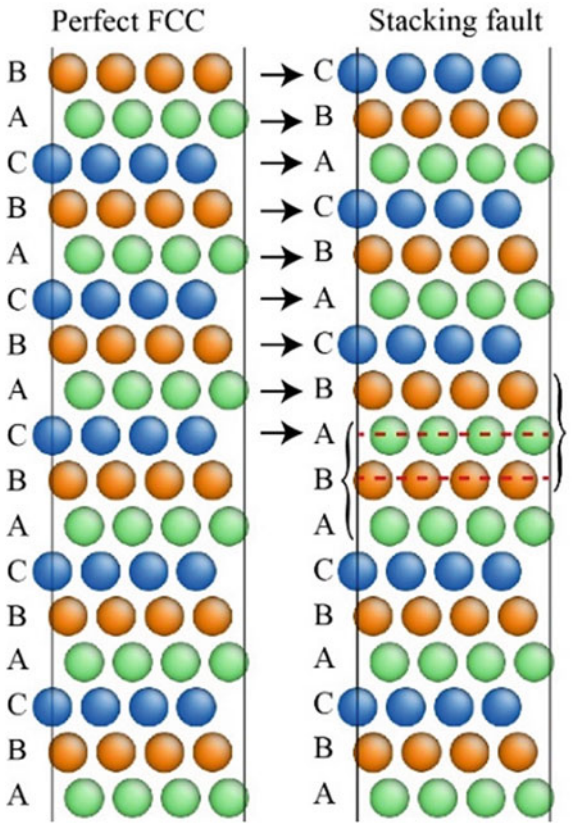

Fig. 5.1 Atomic models for SF energy calculation in FCC metals

the energy barrier. First principles calculations satisfactorily reproduce the experimental values. Moreover, first principles calculations are superior in predicting the SF energy of transition states during the whole slip motion. Even though it is generally difficult for an empirical potential composed of a two-body functional to reproduce high SF energy, some EAM potentials have been found to demonstrate excellent characteristics to describe the dislocation core in FCC metals.

In HCP metals, it is more effective to understand the SF energy because the slip behavior is more complicated than that of cubic crystals. In general, plastic deformation in HCP metals is caused by dislocation of the slip and twinning deformation modes. Focusing on the slip mode, <a> and <c + a> dislocations can glide in basal, prismatic, and pyramidal planes. All possible slip systems are given in Fig. 5.3, where <a> dislocation can glide in basal, prismatic and first-order pyramidal planes, and <c + a> dislocation in first- and second-order pyramidal planes. An overview of the generalized SF energy on each plane is given in Fig. 5.4, where Mg was chosen as a typical example of HCP metals. Several tens of node points on each slip plane are chosen for the sampling data and the energy was evaluated by first principles calculations. The direction and SF energy along the minimum energy path (shown by the

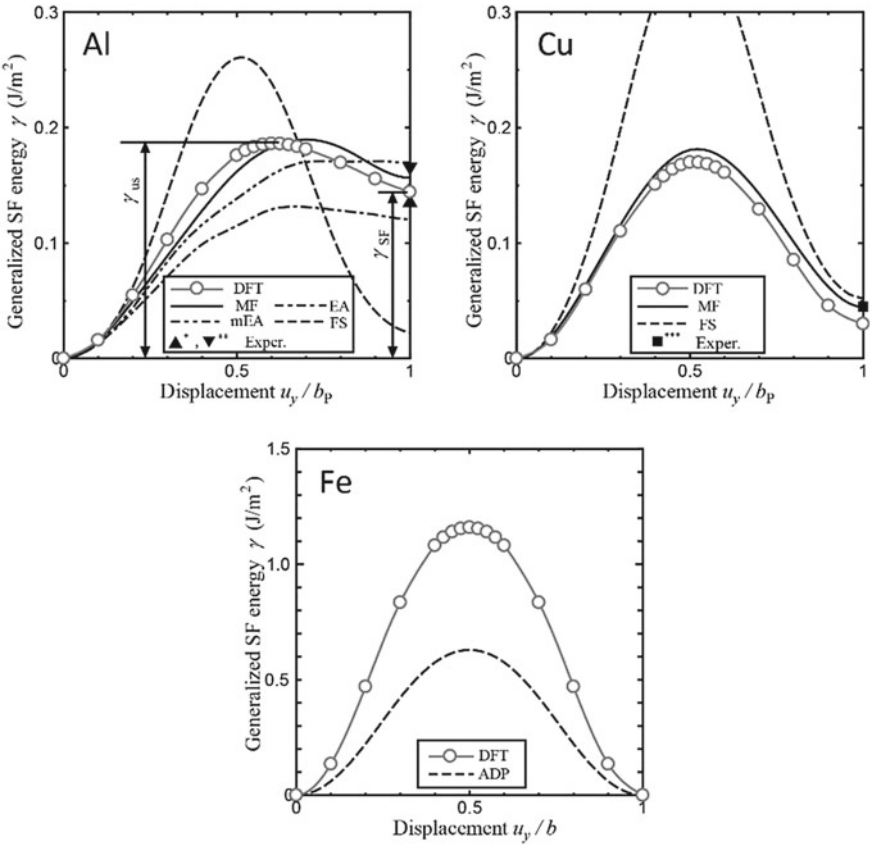

Fig. 5.2 Generalized SF energy curves along the Burgers vector in Al, Cu and Fe, calculated by first principles calculations and some empirical potentials. MF, EA, mEA, FS, and ADP correspond to the empirical potentials proposed by Mishin–Farkas (Mishin et al. 1999, 2001), Ercolessi–Adams (Ercolessi and Adams 1994), modified EA (Liu et al. 1996), Finnis–Sinclair (Finnis and Sinclair 1984), Angular dependent potential (Mishin et al. 2005). *, ** and *** are experimental values cited by the literature (Dobson et al. 1967; Murr 1975; Hirth and Lothe 1982)

red arrows) on the slip plane is the most important for determining the dislocation motion because the direction corresponds to the Burgers vector of each slip plane. In case of the basal slip, the <a> dislocation tends to dissociate into a partial dislocation and the Burgers vectors are given as those of two partial dislocations according to the minimum energy path. However, <a> dislocation in the prismatic plane does not dissociate into partials.

The basal <a> , prismatic <a> , pyramidal I <a> , pyramidal I <c + a> , and pyramidal II <c + a> slip systems can be considered as the only possible slip systems except for twin modes. Figure 5.5 shows the energy difference along the minimum energy path of all slip systems in Mg, Zn, Ti, and Zr as typical HCP metals. The c/a ratio of these HCP metals, calculated by first principles, are 1.613, 1.886, 1.582, and

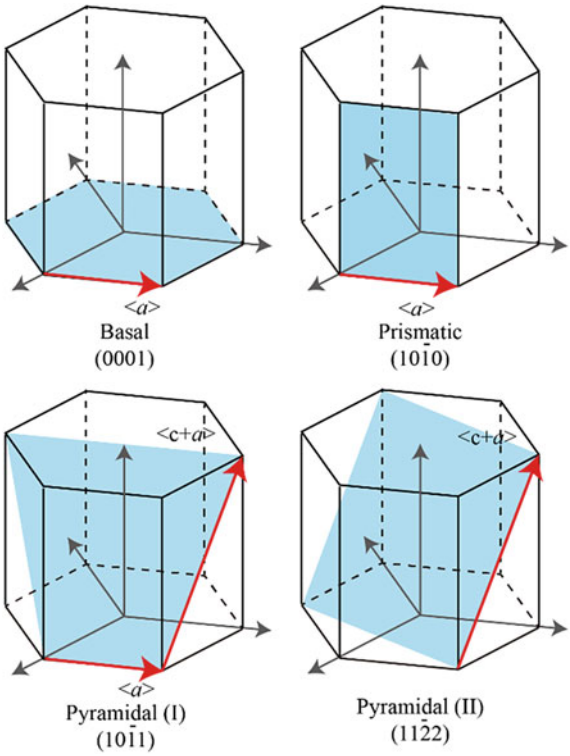

Fig. 5.3 Possible slip systems of <a> and <c + a> dislocations in basal, prismatic, first- and second-order pyramidal planes. The red arrow indicates the direction of each Burgers vector

1.598 for Mg, Zn, Ti, and Zr, respectively. In the case of Mg and Zn, the SF energy of the <a> slip in the basal plane is much lower than those of any other non-basal slip planes, and the basal <a> slip is a primary slip system in these metals. In contrast, the SF energy of the <a> slip in the prismatic plane is the lowest and the prismatic <a> slip is the primary slip system. These tendencies can be understood using structural information, that is, c/a is among the simplest indicators that provides a favorable slip plane and direction. The SF energy in the basal plane tends to decrease when the c/a ratio is larger than the ideal c/a ratio. On the contrary, the prismatic <a> becomes the primary slip system when the ratio is smaller than the ideal. However, the SF energy is more important for understanding the detailed information of the slip system in HCP metals.

5.3 Analytical Description of Dislocations: Peierls–Nabarro Model

As discussed above, the SF energy calculation provides useful information for the dislocation core and motion. However, the SF energy can only give an interfacial

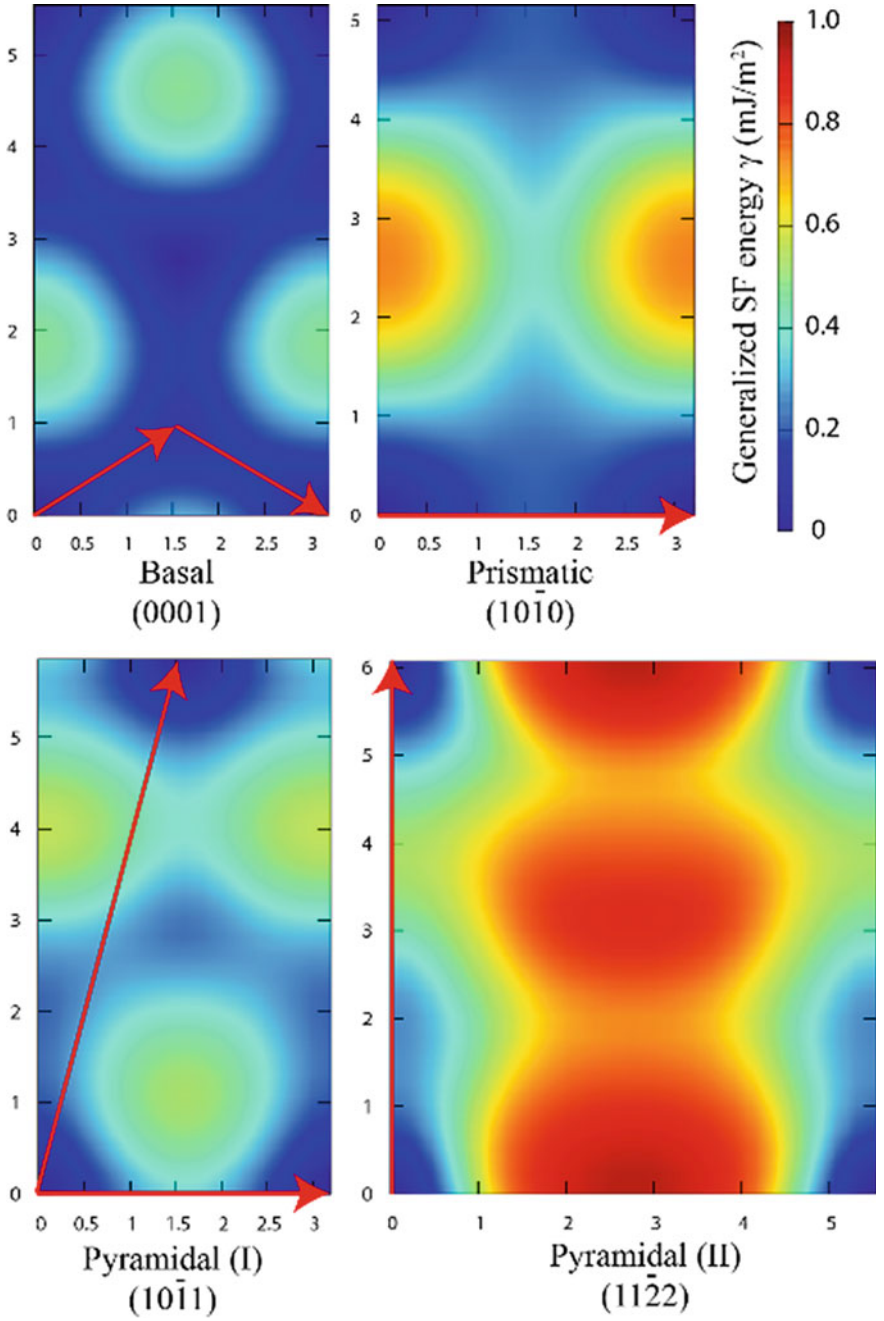

Fig. 5.4 Generalized stacking fault energies on a possible slip plane in Mg. All data were evaluated by first principles calculation. The minimum energy path is indicated by the red arrow, which corresponds to the direction of each Burgers vector

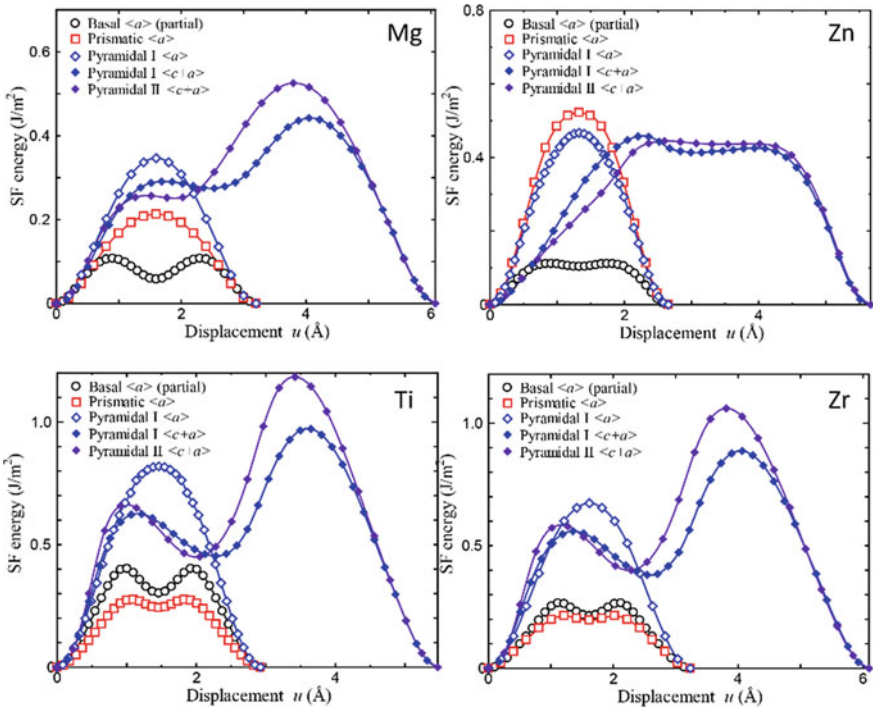

Fig. 5.5 Generalized stacking fault energies along the minimum energy path in all possible slip planes in Mg, Zn, Ti, and Zr. Here, the basal <a> , prismatic <a> , pyramidal I <a> , pyramidal I <c + a>, and pyramidal II <c + a> slip systems are considered as the possible slip systems

misfit energy of the dislocation core, which is not enough to capture a comprehensive picture of the dislocation because the elastic strain energy around the dislocation core should be considered. The self-energy of the dislocation should be described by a combination of the contributions of both the elastic energy generated by the local disconnection of the core region and the interfacial misfit energy. Peierls (Peierls 1940) and Nabarro (Nabarro 1947) first considered a simplified description of the dislocation core in a two-dimensional lattice as shown in Fig. 5.6 and proposed the Peierls–Nabarro (PN) model. Here, the dislocation core can be expressed by the two elastic semi-infinite bodies and the non-linear interplanar misfit at the interface of two bodies.

In the PN model, the relative displacement between two lattice planes at the interface is defined by the lattice mismatch (disregistry), and the disregistry is allowed to have a distribution of displacement along the direction of Burgers vector. The total displacement of the disregistry can be considered using a set of local components of displacement $\delta(x)$, which corresponds to the dislocation segment with an infinitesimal Burgers vector. The local gradient generated by the disregistry is defined by dislocation core density $\rho(x)$ as follows:

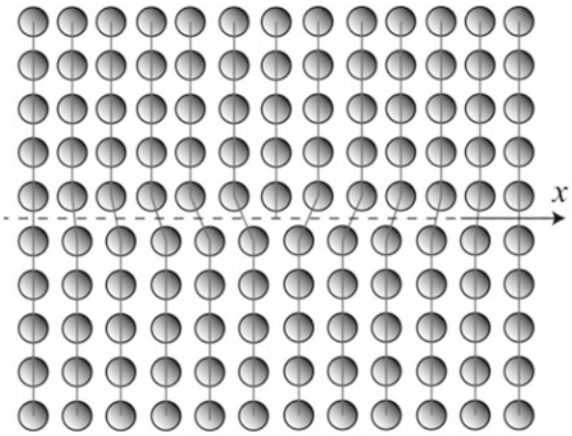

Fig. 5.6 Schematic image of a pure edge dislocation core in a two-dimensional lattice

$$db(x) \equiv \rho(x)dx, \quad \rho(x) = \left(\frac{d\delta(x)}{dx}\right). \tag{5.2}$$

Here, the integral along the x direction within the infinite region is equal to the Burgers vector. The following PN equations hold when the stress generated by the disregistry is balanced against the interfacial restoring force F.

$$\frac{K}{2\pi}\int_{-\infty}^{\infty}\frac{\rho(x')}{x-x'}dx' = F(\delta(x)), \tag{5.3}$$

where K is the energy factor corresponding to the elastic coefficient and given for isotropic media (Foreman 1955).

$$K = \frac{\mu}{2\pi}\left(\frac{\sin^2\theta}{1-\nu} + \cos^2\theta\right), \tag{5.4}$$

where μ and ν are the shear modulus and Poisson's ratio, respectively. θ is the angle between the dislocation line and Burgers vector. This PN equation is solved analytically on the assumption that the restoring force can be described by an analytic function such as the sinusoidal function. Similarly, the total energy of dislocation can be expressed by the local elastic interaction generated by the infinitesimal dislocation segments, long-range elastic interaction, and misfit potential at the interface of two bodies.

$U_{\text{tot}}[\rho(x)] = U_{\text{elastic}} + U_{\text{misfit}} + U_{\text{long}},$. (5.5)

$$U_{\text{elastic}} = -\frac{K}{4\pi}\int_{-\infty}^{\infty}\int_{-\infty}^{\infty}\rho(x)\rho(x')\ln|x-x'|dxdx'. \tag{5.6}$$

$$U_{\text{misfit}} = \int_{-\infty}^{+\infty} \gamma(\boldsymbol{\delta}(x))dx. \tag{5.7}$$

The long-range interaction is given analytically by the classical theory of dislocations. Accordingly, the total energy of the dislocation can be expressed by a functional of the disregistry and its derivative, that is, dislocation core density. Therefore, a stable configuration of a dislocation is obtained using the variational of this energy functional. Joós and Duesbery developed an analytical model based on the PN model to estimate the Peierls stress for wide and narrow dislocations by introducing the generalized SF energy, its maximum gradient, and the dislocation half-width (Joós and Duesbery 1997). It should be noted that the Peierls stress evaluated by the analytical function based on the PN model is solved on the assumption that the dislocation is dissociated along the one-dimensional direction only and that the estimation depends on the accuracy of the maximum restoring force.

Recently, a sophisticated model of the semi-discrete variational (SV) PN model (Bulatov 1997; Lu et al. 2000) was developed, which provides information on the three-dimensional local structure of a dislocation core and the Peierls stress through discretized atomic rows and the reliable GSF energy surface (so-called γ surface) determined by DFT. In the SVPN framework, the total fault energy of a dislocation under external stress can be described similarly by $U_{tot} = U_{\text{elastic}} + U_{\text{misfit}} + U_{\text{stress}}$, where long-range interaction is excluded. The first term is the configuration-dependent elastic energy is as follows:

$$U_{\text{elastic}} = \sum_{i,j} \frac{1}{4\pi} \chi_{ij} [K_{\text{e}}(\rho_i^{(1)}\rho_j^{(1)} + \rho_i^{(2)}\rho_j^{(2)}) + K_{\text{s}}\rho_i^{(3)}\rho_j^{(3)}], \tag{5.8}$$

where, $\rho_i^{(1)}$ and $\rho_i^{(2)}$ are related to the edge component and $\rho_i^{(1)}$ is related to the screw component, K_{e} and K_{s} are associated with the energy factor evaluated by Eq. (5.3), and χ_{ij} is defined in the literature (Bulatov 1997; Lu et al. 2000). The second term is the interfacial energy described by the total sum of nodes:

$$U_{\text{misrit}} = \sum_i \Delta x \gamma(\delta_i). \tag{5.9}$$

The third term represents the work done by the plastic deformation through the dislocation glide. Here, all terms can be expressed as the discretized the functions of disregistry vector and the core density of dislocation. According to the displacement of each atomic row x_i, the disregistry and core density are related to $\rho_i = (\delta_i - \delta_{i-1})/(x_i - x_{i-1})$, which is associated with the local gradient of relative displacement. In accordance with the classical PN model, the stable configuration of the dislocation core can be evaluated numerically by minimizing the variational function to find the stable configuration of the disregistry (or the dislocation core density).

The basal and prismatic <a> dislocations in HCP Mg alloys are taken as an example of good application of the SVPN framework. First, atomic configurations

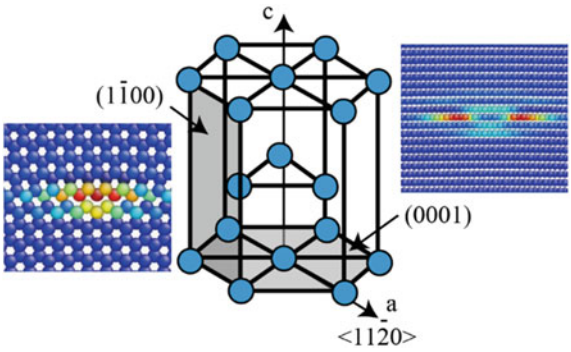

Fig. 5.7 Unit cell of hexagonal crystal and the core structures of the basal and prismatic <a> dislocations from molecular statics simulations (Tsuru et al. 2013). Reprinted from J. Phys: Condens. Matter., vol. 25, Tsuru et al., Fig. 1a, Copyright (2020), with permission from IOP

of both dislocations were investigated by atomistic simulations. The crystallographic orientation and corresponding atomic configurations are shown in Fig. 5.7. A fully-atomistic molecular statics simulation was performed using the EAM potential proposed for Mg (Sun et al. 2006). The atoms were visualized using the ATOMEYE visualization software (Li 2003). The fully-atomistic simulations confirmed that a basal dislocation tends to dissociate into two partial dislocations with wide stacking fault while the core width of a prismatic dislocation is narrow. The energy differences with respect to the in-plane displacement along the minimum energy path (slip direction) in the basal and prismatic planes evaluated by the density functional theory (DFT) calculation and EAM potential are shown in Fig. 5.8. The DFT data were the same as shown in Fig. 5.5 while the energy landscape along the slip direction of both the basal and prismatic planes had similar characteristics. It is noted that the direction of minimum energy path in the prismatic plane varied slightly (Tsuru et al. 2013), and the differences of the generalized SF energy as well as the elastic properties reflected the dislocation core structure.

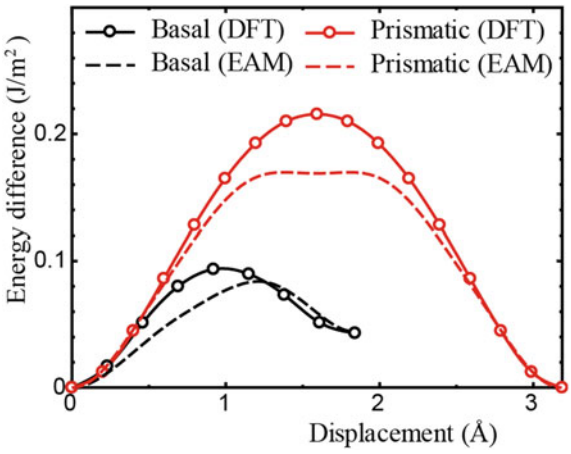

Fig. 5.8 Generalized SF energy along the minimum energy path evaluated by DFT and the EAM potential (Tsuru et al. 2013). Reprinted from J. Phys: Condens. Matter., vol. 25, Tsuru et al., Fig. 1 (c), Copyright (2020), with permission from IOP

The energy factors for the pure edge and screw dislocations in the basal and prismatic planes of magnesium were evaluated directly by DFT and the EAM potential, as summarized in Table 5.1. The anisotropic shear modulus is the value of the slip direction, i.e., C_{44} and C_{66}. Poisson's ratio is assumed to be evaluated by orthogonally transformed anisotropic elastic constants through the direction cosine and the Voigt average.

All material properties of Mg are applied to SVPN analysis. The core densities of the basal and prismatic <a> dislocation, calculated by SVPN analysis combined with DFT calculations and the EAM potential, are summarized in Fig. 5.9. Two peaks

Table 5.1 Energy factors calculated by first principles and the EAM potential for the evaluation of the elastic energy of the dislocation core (Tsuru et al. 2013). Reprinted from J. Phys: Condens. Matter., vol. 25, Tsuru et al., Table 1 (c), Copyright (2020), with permission from IOP

	Basal <a>		Prismatic <a>	
	K_e (GPa)	K_s (GPa)	K_e (GPa)	K_s (GPa)
DFT	3.88	2.93	4.10	2.98
EAM	2.49	2.03	4.55	3.52

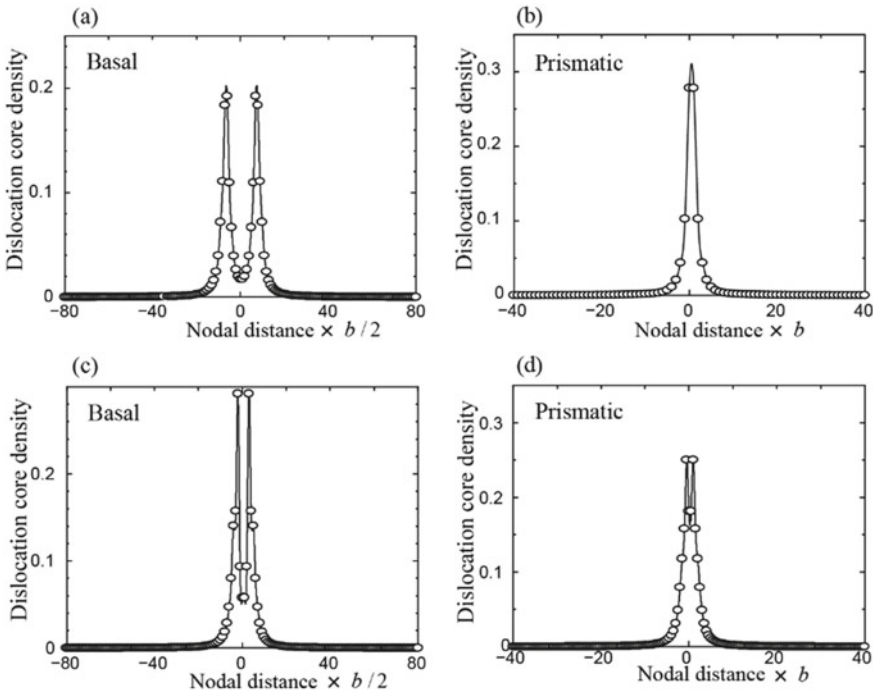

Fig. 5.9 Dislocation core densities in the basal and prismatic planes, evaluated by the SVPN model with (a, b) using DFT, and (c, d) using the EAM potential (Tsuru et al. 2013). Reprinted from J. Phys: Condens. Matter., vol. 25, Tsuru et al., Fig. 2, Copyright (2020), with permission from IOP

of the core density of the basal dislocation represent the dissociated two partial dislocations associated with the low stacking fault energy of Mg. The difference in the width of extended dislocation between DFT and EAM are affected by the meaningful difference of the energy factor, as shown in Table 5.1. The core density of dislocation in the prismatic plane evaluated by DFT distributes sharply while that of EAM slightly dissociates into two peaks, which is definitely reflected by the difference of generalized SF energy. The Peierls stresses were 1 MPa and 49 MPa for the basal and prismatic <a> dislocations, respectively. Additionally, as an example, SVPN analysis is applied to the prismatic <c> dislocation, which is not a slip system of HCP metals. SVPN analysis confirmed that the Peierls stress of the prismatic <c> dislocation was extremely high (1.49 GPa).

The non-basal slip is thought to be key to improving the ductility in Mg alloys. Thus, the effect of the alloying element is the subject of research and interest. The SVPN model has the potential to capture how alloying elements influence the dislocation core structure and the Peierls stress. As a typical example, the effect of yttrium solution on the dislocation core structure and the critical stress of the motion of prismatic <a> dislocation (i.e., Peierls stress) were discussed here. When an isolated solute atom was substituted for a magnesium atom on the slip plane, the influence of the solution element on the generalized SF energy and the restoring force are shown in Fig. 5.10. The effect of yttrium solution at different concentrations was investigated, and aluminum was chosen for comparison, which is a typical solute element of magnesium alloys such as the AZ31 alloy. The restoring force was defined as the gradient of the GSF energy along the minimum energy path, and its maximum value, denoted by $\tau_{\max}$, is related to the dislocation half-width through the analytical PN model (Joós and Duesbery 1997). The energy difference was remarkably reduced by yttrium solution, and in this regard the maximum restring force fell to one-half that of pure magnesium. However, aluminum solution raises the energy gradient and the restoring force, and zinc solution was found to show a tendency similar to that of aluminum. The dislocation core structures in case that yttrium is substituted in the slip plane, was calculated by the SVPN analysis as shown in Fig. 5.11. The dislocation tends to spread as the solute concentration increased because the contribution of the elastic interaction became relatively large owing to the reduction of the gradient of the GSF energy. The resultant Peierls stresses were reduced to 14 MPa and 8 MPa for 11 at.% and 25at.% yttrium solution concentration, respectively. Thus, yttrium solute results in the alteration of the dislocation core structure and lubrication of the dislocation motion (Tsuru et al. 2013).

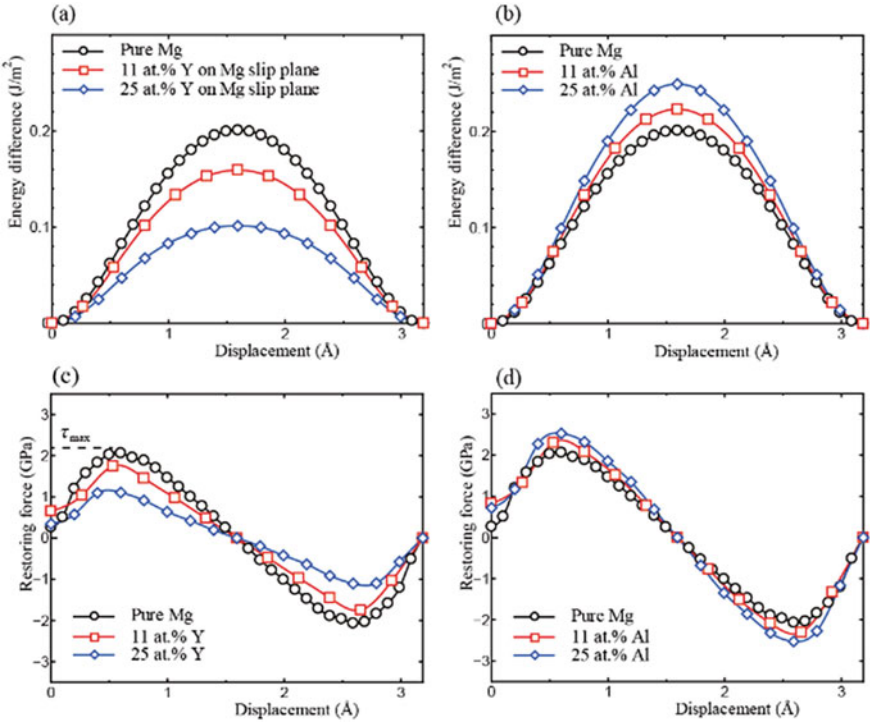

Fig. 5.10 Stacking fault energies and restoring forces in the case where a solution element is placed on the slip plane compared with those of pure magnesium. **a** and **c** correspond to yttrium solution. **b** and **d** correspond to aluminum solution (Tsuru et al. 2013). Reprinted from J. Phys: Condens. Matter., vol. 25, Tsuru et al., Fig. 3, Copyright (2020), with permission from IOP

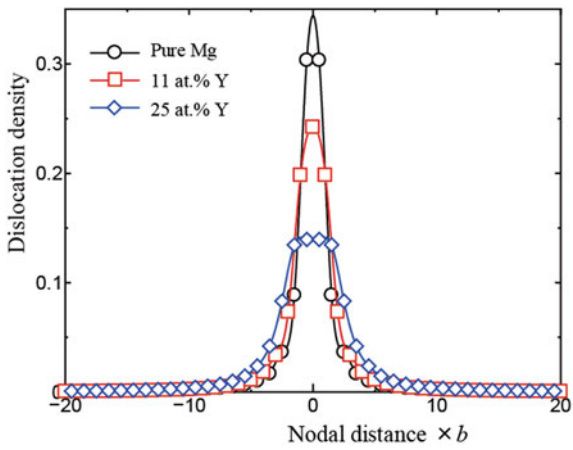

Fig. 5.11 Effect of yttrium solution at several solution concentrations on the dislocation core density (Tsuru et al. 2013). Reprinted from J. Phys: Condens. Matter., vol. 25, Tsuru et al., Fig. 4, Copyright (2020), with permission from IOP

5.4 First Principles Calculations of a Dislocation Core

5.4.1 Atomic Modeling of a Dislocation Core

The effect of solute atoms on the dislocation motion is characterized by not only the SF energy but also by the elastic and chemical interactions around the dislocation core. Recently, various defect structures, such as the vacancy impurity cluster and grain boundary, can be treated directly by first principles calculations, and many fundamental properties have been extracted. However, band structure calculations, i.e., the DFT calculations based on plane-wave basis sets for the wave function of electrons, are generally solved under the period boundary condition, in which special attention is required in handling defect structures in a small supercell (up to several hundreds of atoms) because the elastic field of defects is generally long-ranged. According to the linear elasticity theory, the elastic field of a vacancy and volumetric defect, such as an impurity cluster, decays with $1/r^3$ (the factor of distance). The stress field of the coincidence site lattice (CSL) grain boundary is also short-ranged. As a result, these defect structures can be modeled successfully by small supercell models. However, according to elasticity theory, the stress field of an isolated dislocation decays according to the factor of $1/r$ (Hirth and Lothe 1982) and, therefore, it is not possible to treat such an isolated dislocation within first principles calculations. Two approaches have been developed to evaluate the dislocation within the first principles framework. One is the flexible boundary condition method, which can capture the long-range strain field of a dislocation by coupling the dislocation core to an infinite harmonic bulk through the lattice Green function. The other is to consider the dislocation dipoles in a periodic cell. The elastic field of the dislocation dipole in a periodic cell can be treated by the superposition of an image dislocation (Cai et al. 2003, 2001) or by considering the elastic field in the reciprocal space (Mura 1964; Daw 2006). The latter is explained as follows.

The dislocation core in a periodic cell is introduced based on the solution of continuum linear elastic theory of the periodic dislocation dipole array (Daw 2006). The displacement gradient caused by the periodic distribution of dislocations is expressed as a Fourier series:

$$\underline{\underline{\Delta}}(\mathbf{r}) = \sum_{\mathbf{G}} \underline{\underline{\tilde{\Delta}}}(\mathbf{G}) \exp(i\mathbf{G} \cdot \mathbf{r}), \tag{5.10}$$

where $\underline{\underline{\Delta}}(\mathbf{r})$ is the displacement gradient tensor at point $\mathbf{r}$, $\mathbf{G}$ is the reciprocal lattice vectors, and $\underline{\underline{\tilde{\Delta}}}(\mathbf{G})$ is the Fourier coefficients describing the displacement gradient tensor. The elastic energy per unit length of the supercell can be expressed in terms the $\underline{\underline{\tilde{\Delta}}}(\mathbf{G})$ s:

$$E_{\text{elastic}} = \frac{1}{2} A_c c_{ijkl} \sum_{\mathbf{G}} \tilde{\Delta}_{ij}(G)\, \tilde{\Delta}^*_{kl}(G), \tag{5.11}$$

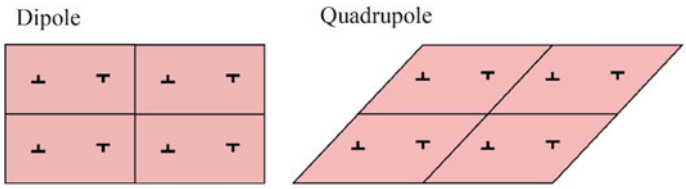

Fig. 5.12 Atomic model of dislocation dipole and quadrupole configurations in a periodic cell

Table 5.2 Lattice parameters and elastic constants in hexagonal Mg

	a (Å)	c/a	c_{11}	c_{33}	c_{12}	c_{13}	c_{44}
DFT	3.203	1.614	62.4	70.9	22.0	21.9	11.7
Exp. (Hearmon 1979)	3.209	1.623	59.3	61.5	25.7	21.4	16.4

where A_c is the area of the supercell perpendicular to the dislocation line and c_{ijkl} are the anisotropic elastic constants. The distortion field can be solved by minimizing the total elastic energy subject to the topological constraints imposed by the dislocation dipole. This theory is found in the literature, and the procedure is solved numerically by a sequence of linear algebra in the reciprocal space (Daw 2006). Subsequently, the displacement can be evaluated by a line integral starting from a reference coordinate in real space, and the local displacement at the atomic positions is provided. In practice, core radius, r_c is introduced to insure convergence of the summation for the elastic energy.

This approach is applied to HCP Mg alloys. The dipole of screw dislocation whose Burgers vectors is type $a/3\langle 11\bar{2}0\rangle$ is treated here. The dislocation is inserted into a 288-atom supercell with 12×6 periodic units along [0001] and $[1\bar{1}00]$, respectively, where the dislocation is inserted as dipolar and quadrupolar configurations, as shown in Fig. 5.12. The elastic constants and lattice parameters for Mg are obtained using density functional theory (DFT). Our computed values are shown in Table 5.2. The (2-D, for this problem) reciprocal lattice vectors can be expressed in terms of the primitive reciprocal lattice vectors, defined to be $\mathbf{a}^*$ and $\mathbf{b}^*$, as $\mathbf{G}_{hk} = h\,\mathbf{a}^* + k\,\mathbf{b}^*$ with $h, k \in Integers$. Seen in the predictions of one component of the displacement gradient tensor as a function of the number of $\mathbf{G}$ vectors in the sum, the Fourier series is completely converged when the core radius r_c is equal to b, and both h and k range from -20 to 20. In this way, the displacement gradient can be solved numerically. The solution of the strain and displacement fields of the dislocation dipolar and quadrupolar configurations evaluated by linear elasticity theory in a periodic cell are shown in Fig. 5.13. The strain field is actually periodic and the displacement field is depicted in the cumulative boundary condition along the y-direction. The method also allows us to estimate the elastic strain energy of dipolar and quadrupolar configurations in terms of the change in the relative displacement of the dislocation pair. The introduction of dislocation dipoles within each supercell results in a distortion of the supercell vectors, as noted by Lehto and Öberg (Lehto and

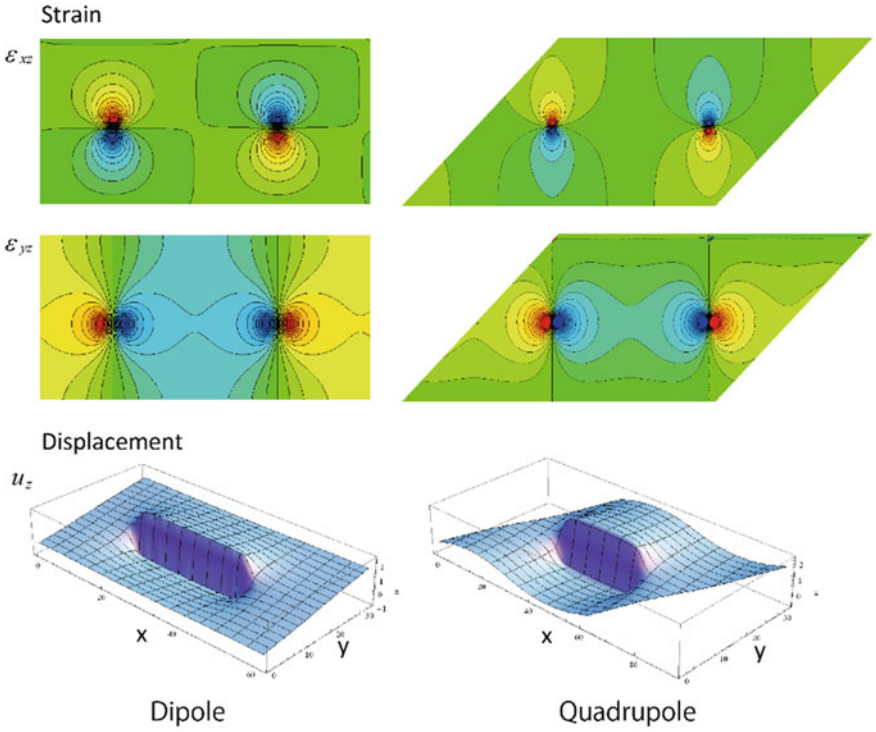

Fig. 5.13 Solution of the strain and displacement fields of the dislocation dipolar and quadrupolar configurations, evaluated by linear elasticity theory in a periodic cell

Öberg 1998). The relationship between strain energy and the relative displacement in the case of the dipolar and quadrupolar configurations in Mg with the above atomic model is given in Fig. 5.14. Here, the energy difference of the quadrupole is less sensitive to the relative displacement than that of the dipole, and therefore the quadrupolar configurations should be chosen for the first principles calculations when a small supercell is used.

5.4.2 First Principles Calculations

The displacements corresponding to each lattice point, obtained using the continuum linear elasticity theory outlined above, were applied to the atomic model for a dislocation dipole in the quadrupolar stacking configuration. In addition, the periodic supercell vectors were adjusted as discussed above. The dislocation core structure so obtained is used as the initial configuration for the first principles calculations. The supercell model of HCP metals is prepared as provided above, and the that of BCC metals is similarly prepared: a 135 atom model with dimensions $\mathbf{a} = 5\mathbf{e}_1$,

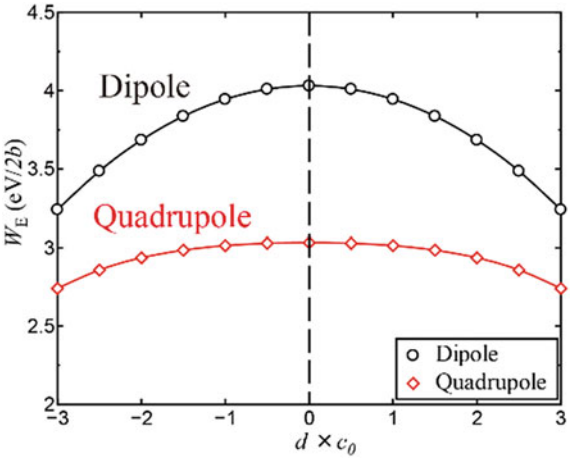

Fig. 5.14 Strain energy depends on the relative displacement when the size of a supercell is applied to the linear elasticity model

$\mathbf{b} = 2.5\mathbf{e}_1 + 4.5\mathbf{e}_2 + 0.5\mathbf{e}_3$, and $\mathbf{c} = \mathbf{e}_3$, where unit vectors in the system are defined as $\mathbf{e}_1 = a_0\left[\sqrt{6}, 0, 0\right]$, $\mathbf{e}_2 = a_0\left[0, \sqrt{2}, 0\right]$, and $\mathbf{e}_3 = a_0\left[0, 0, \sqrt{3}/2\right]$, with a coordinate system corresponding to the $x = [11\bar{2}]$, $y = [1\bar{1}0]$ and $z = [111]$ directions.

First principles calculations were then implemented to determine the structural relaxation. The stable configuration of the dislocation core structures in typical BCC and HCP metals is shown in Fig. 5.15, where the left side of the dislocation is depicted by the differential displacement (DD) vector (Vitek et al. 1970; Vitek 1974), and the core structures in BCC Fe, Nb, Mo and HCP Mg, Ti, Zr are provided as the typical examples. It is obvious from Fig. 5.15 that the dislocation core of BCC metals is compact owing to the high SF energy, as shown in Fig. 5.2. In addition, there is little difference in the dislocation core structures depending on the type of element in BCC metals. However, the core structures of HCP metals differ completely depending on type. As discussed in Sect. 5.2, dislocations of HCP metals tend to be dissociated according to the SF energy. The dislocation of Mg is dissociated in the basal plane due to the small SF energy in its plane while that of Zr dissociated in the prismatic plane. On the contrary, the dislocation of Ti is dissociated in the first-order pyramidal $(10\bar{1}1)$ plane. Pyramidal <a> dislocations cannot be activated because the SF energy along the <a> direction in the pyramidal $(10\bar{1}1)$ plane is generally extremely high. However, a unique core structure was recently discovered where the <a> dislocation is more likely to dissociate in the dense $(10\bar{1}1)$ plane than in prismatic plane because the SF energy, when the displacement is half the Burgers vector along the <a> direction in the dense $(10\bar{1}1)$ plane, is slightly smaller than that of the prismatic plane (Clouet et al. 2015). Thus, HCP metals have a wide variety of dislocation core structures, including various <a> dislocations and <c + a> dislocations in the first and second-order pyramidal planes, reflecting the SF energy, as shown in Fig. 5.5. As a result, plastic deformation in HCP metals becomes more complicated, i.e., solute atoms play a more significant role in the change in the slip mode through the electronic interactions between matrix elements and solutes.

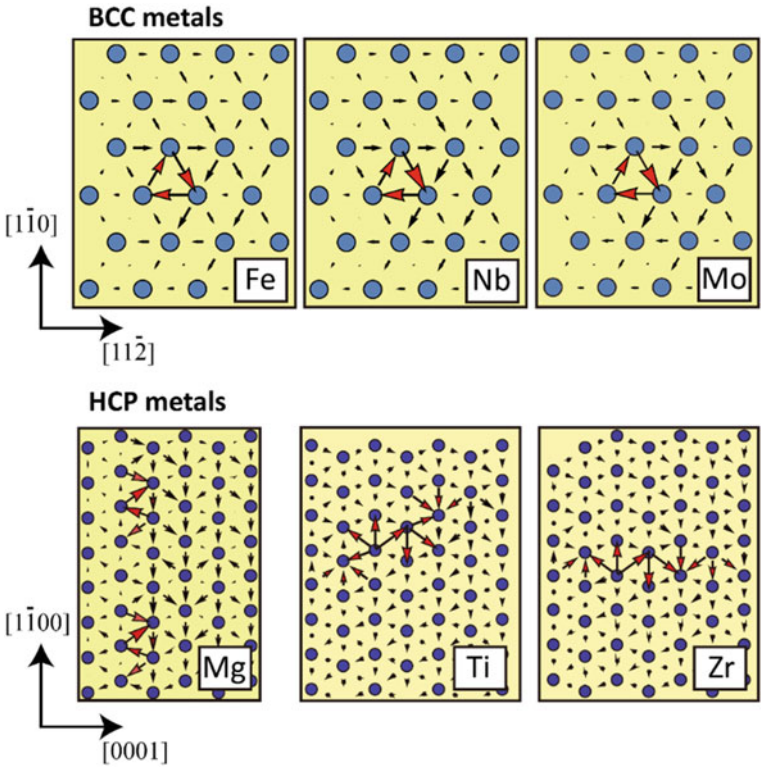

Fig. 5.15 Stable configurations of the dislocation core in BCC Fe, Nb, Mo, and HCP Mg, Ti, Zr, evaluated by first principles calculations. The relative displacement associated with the nearest neighbor atom was visualized by a DD vector

At the end of this section, the influence of solute atoms on the dislocation core structure and motion in Mg alloys is taken as an example. When the stable configuration was obtained, the energy barrier for the dislocation motion (i.e., Peierls potential) by first principles calculations attracts interest. The nudged elastic band (NEB) method (Henkelman et al. 2000) was employed to evaluate the electronic structure of the dislocation core when it overcomes the Peierls barrier. Initial configurations were prepared corresponding to the most stable structure position and the position where a dislocation moves through the Peierls barrier. The energy difference during dislocation glide of the left side of the dislocation on the basal, prismatic, and pyramidal planes, as well as the DD map at intermediated transition states, are shown in Fig. 5.16. It is confirmed that the screw dislocation dissociates into partial dislocations on the basal plane, which is caused by the nature of low SF energy of the basal plane in Mg. It is easy for this type of basal dislocation to glide on the basal plane—there is a negligibly small energy barrier between the symmetrically equivalent structures during basal slip. However, the prismatic slip requires surmounting high energy barrier by NEB calculation. The prismatic slip can be divided into three

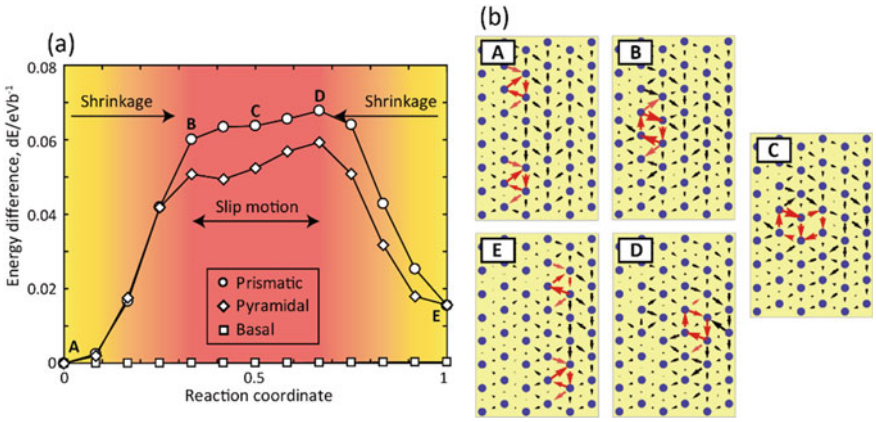

Fig. 5.16 Energy and core structure during the dislocation motion. **a** The minimum energy paths are for the motion of the screw dislocation in the basal, prismatic and pyramidal planes. **b** Intermediate transition states for prismatic slip visualized by the DD map (Tsuru and Chrzan 2015). Reprinted from Sci. Rep., vol. 5, Tsuru et al., Fig. 2

steps which is consistent with the Friedel–Escaig mechanism proposed by Couret and Caillard (Couret and Caillard 1985). At first, dissociated dislocation on the basal plane constricts that yields the compact core screw dislocation capable of gliding on the prismatic plane. Then, the dislocation with the compact core glides on the prismatic plane. Afterward, a compact core redissociates into partial dislocations on the basal plane. It is evident from Fig. 5.16 that a dominant part of the energy barrier for the prismatic slip is the energy for the constriction of two partial dislocations which enables to cross-slip.

This energy barrier is approximately 0.06 eV/*b*, with *b* being the Burgers vector of <a> dislocation. In contrast, the energy barrier for the glide of the compact core of screw dislocation is much lower, approximately 0.01 eV/*b* for both prismatic and pyramidal glide.

The energy barrier computed in this way has two general contributions: (I) the energy barrier for the motion of an isolated dislocation and (II) the changes to this barrier arising from the interaction with the periodic images. The contribution (II) needs to be considered rightly due to an artifact of the supercell geometry. As shown in Fig. 5.14., Daw's formulation of the periodic elasticity problem (Daw 2006) can be applied to estimate the changes in elastic energy within a periodic supercell as the dislocation moves between A and E. The linear elastic description of the periodic supercell enables to discern the effects of the periodicity on the computed Peierls barrier. According to elasticity theory, the contribution of the energy barrier as a function of supercell size can be drawn by Daw's formulation which found to be eliminated by considering in the large supercell limit (~18,000 atoms) (Tsuru and Chrzan 2015).

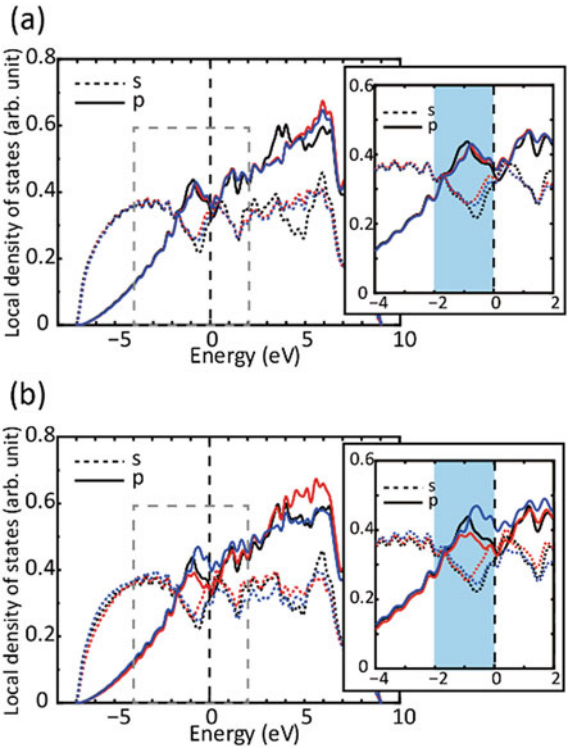

Fig. 5.17 Electronic structure of **a** the dissociated and **b** the compact dislocations in Mg. The projected DOS around the core is indicated by red and blue lines and that of the perfect crystal is indicated by a black line. Dotted lines and solid lines indicate *s*- and *p*-states, respectively. Energy states with respect to the energy range from −4.0 to 2.0 eV are shown in the inset (Tsuru and Chrzan 2015). Reprinted from Sci. Rep., vol. 5, Tsuru et al., Fig. 3

Returning to the quantum formulation of the problem, the changes in the electronic structure associated with the dislocation motion along the prismatic plane. The electronic structures of the initial and the sixth intermediate configurations corresponding to the partial and compact dislocations, are shown in Fig. 5.17. The site-projected density of states (DOS) on the two atom positions around the dislocation core for the dissociated and compact cores corresponding to states A and C in Fig. 5.16 was examined as well as the atom in the perfect crystal. Thus, the evolution of the site-projected DOS as the dislocation passes over the Peierls barrier can be captured.

As presented in Fig. 5.17, analyzing the DOS establishes two points. First, the states of the outermost *s* electrons of Mg do not change significantly in the dislocation core. Second, the passage of a dislocation is influenced strongly by the *p*-states just below the Fermi level. The DOS around a site of core region is reduced by the compact dislocation while the projected DOS for the other site is increased, which means the DOS changes slightly when the dislocation forms unstable compact core. Even if the change of DOS is not so significant, the rearrangements are much more pronounced in the case of the compact core. Furthermore, these *p*-states participate in the bonding rearrangements that take place as the core transitions from partials to a compact core to surmount its Peierls barrier. The changes of the electronic structure as it surmounts its Peierls barrier constitute the electronic structure during the dislocation motion.

It is thus interesting to identify substitutional elements which is expected to interact significantly with the dislocations.

The principle underlying our analysis is not so complicated. Just see how the electronic structure changes when a substitutional solute is introduced around a dislocation core. It is expected that a strong chemical hybridization can exist between electronic states of solute atom and Mg atoms around solute and dislocation core if the changes occur in the same energy range associated with them. To explore this idea, the electronic structures of Al, Zn, Y, Ca, Ti, and Zr substitutional atoms within Mg were examined. Figure 5.18 shows the site-projected DOS of various solutes around the core. Here, Al and Zn have small effect on the electronic states in the energy range (−2–0 eV) which is important for the motion of the dislocation. In contrast, Y, Ca, Ti, and Zr are found to have relatively large changes in this energy range. Therefore, it is expected that substitutional Y, Ca, Ti, and Zr have strong interaction with the dislocation motion while Al and Zn will not.

The interaction of the dislocation with substitutional solute atoms can be considered directly based on this analysis. Figure 5.19 provides a typical comparison between solutes. Even if the Al solute is added around core region, the dislocation remains dissociated partial dislocations as the Al solute does not influence the

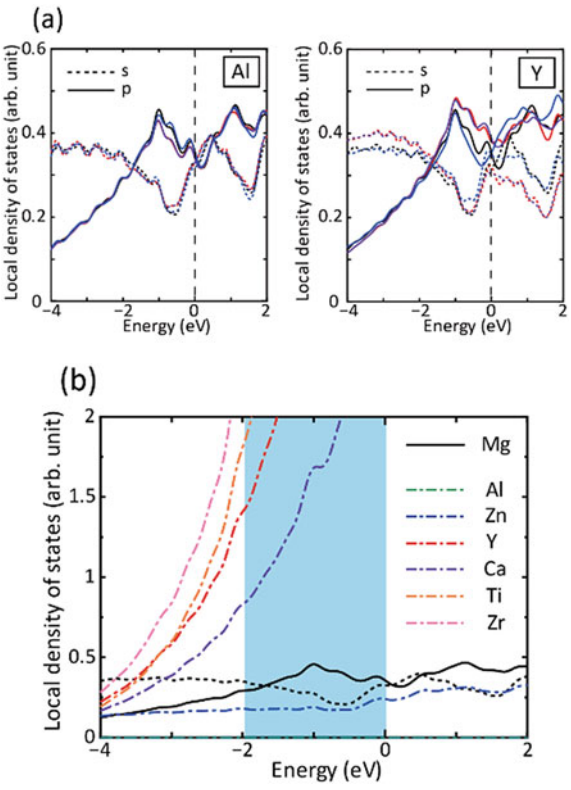

Fig. 5.18 Electronic structure of Mg and a solute in a defect-free crystal. **a** Projected DOS for three atoms around Al and Y solutes. Curves for the perfect region are shown with black lines. **b** DOS for solute elements (Al, Zn, Y, Ca, Ti, and Zr) in a defect-free crystal (Tsuru and Chrzan 2015). Reprinted from Sci. Rep., vol. 5, Tsuru et al., Fig. 4

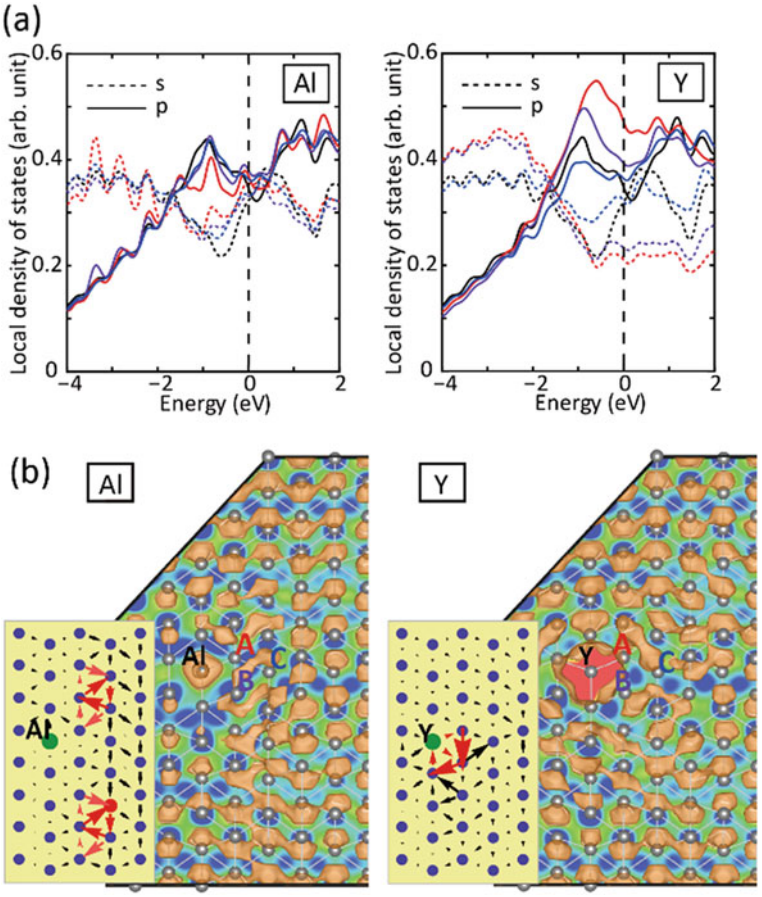

Fig. 5.19 Local electronic structure of the dislocation core around a solute. **a** Projected DOS for atoms constituting the dislocation core. **b** DD map and partial charge density for the dislocation core with a solution with respect to a specific energy range (−2.0–0 eV) (Tsuru and Chrzan 2015). Reprinted from Sci. Rep., vol. 5, Tsuru et al., Fig. 5

electronic states near the dislocation core. In contrast, due to Y solute which have a strong interaction make a dissociated dislocation in the basal plane shrink immediately. Of note, the partial charge density for a dislocation core with Al and Y shows a similar distribution to those for a dissociated and compact dislocation cores, respectively, in pure Mg. Figure 5.19a shows the DOS of Al and Y solutes, where the *s*- and *p*-states of Mg and the *d*-states of each solute element are given in the same graph.

There is clear difference between two types of elements: Al and Zn have no or few *d*-states in the energy range of interest. In contrast, Y, Ca, Ti, and Zr show prominent *d*-states below the Fermi level. These *d*-states are possible for hybridization with the *p*-states of the Mg, and ultimately lead to a strong interaction between these alloying additions and the dislocation core structure. These calculations, therefore, confirm

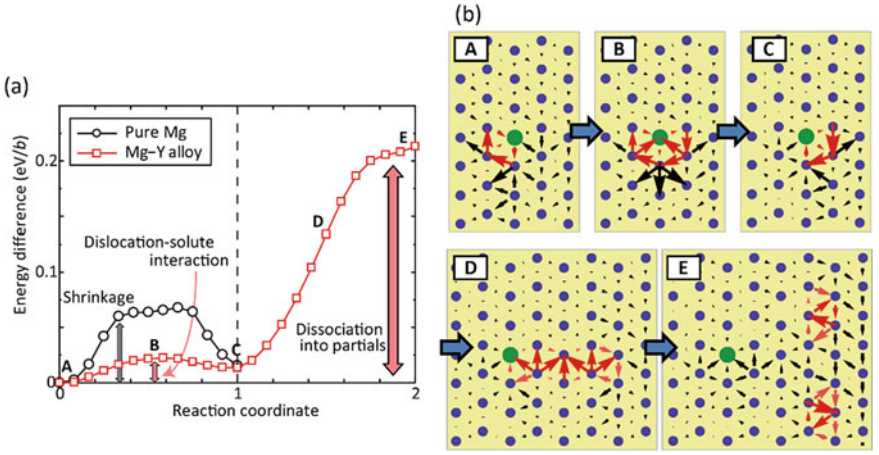

Fig. 5.20 Effect of a solid solution strengthening and softening. **a** Energy differences during the dislocation motion in the prismatic plane in pure Mg and an Mg–Y. The energy curve when the dislocation passes through the Y solution is indicated by the red line. **b** Core structure during the dislocation overcoming and moving away from the Y solution (Tsuru and Chrzan 2015). Reprinted from Sci. Rep., vol. 5, Tsuru et al., Fig. 6

that the electronic structure of the dislocation motion can be applied to identify alloying elements that interact strongly with the dislocations in Mg.

In pure Mg, the glide of a screw dislocation in the prismatic plane is only possible when the dislocation has the compact core configuration as described above. According to the electronic structure calculations show, solutes with the strong interaction bind to, and thus stabilize the compact core. To confirm this scenario, the NEB calculation was reemployed, in which a column of Mg atoms was replaced by Y atoms and the results are shown in Fig. 5.20. Figure 5.20 provides two important observations. First, Y solute results in the core transformation from dissociate partials to compact core when Y is located around dislocation core region. Second, the influence of Y solute is relatively wide-ranged, approximately 3/2 c in all directions. Third, the interaction between Y and dislocation is quite significant, which increase the energy barrier for the basal slip.

Again, plastic anisotropy is one origin of the poor ductility in Mg. In the absence of solute atoms, screw dislocations glide frequently on the basal plane, whereas the energy barrier for non-basal slip are quite high. This plastic anisotropy can be improved if the strength of basal plane slip increases and non-basal slip becomes more frequent. Some solutes found to have a great potential to increase the barrier for basal slip as decreasing the barrier of non-basal slip. It becomes more important to capture the chemical interaction between the dislocation and solutes from the electronic structure basis (Tsuru 2017).

In summary, dislocation motion has been recognized as one of the most important plastons to determine macroscopic plastic deformation. In this section, several

approaches were introduced to capture the dislocation core structure and dislocation-related properties through first principles calculations. These approaches have great potential in the understanding of the fundamental role of dislocation in plastic deformation grounded in electronic structure calculations.

Acknowledgements T.T acknowledges the support of JST PRESTO Grant Number JPMJPR1998 and JSPS KAKENHI (Grant Numbers JP19K04993, JP18H05453). Simulations were performed on the large-scale parallel computer system with SGI ICE X at JAEA.

References

Bulatov VV (1997) Phys Rev Lett 78:4221
Cai W, Bulatov VV, Chang J, Li J, Yip S (2001) Phys Rev Lett 86:5727
Cai W, Bulatov VV, Chang J, Li J, Yip S (2003) Philos Mag 83:539
Carter CB, Holmes SM (1977) Philos Mag 35:1
Clouet E, Caillard D, Chaari N, Onimus F, Rodney D (2015) Nature Mater 14:931
Couret A, Caillard D (1985) Acta Metall 33:1447
Daw MS (2006) Comput Mater Sci 38:293
Dobson P, Goodhew P, Smallman R (1967) Phil Mag 16:9
Ercolessi F, Adams JB (1994) Europhys Lett 26:583
Finnis MW, Sinclair JE (1984) Philos Mag A 50:45
Foreman AJE (1955) Acta Metall 3:322
Hearmon RF (1979) The elastic constants of crystals and other anisotropic materials. In: Hellwege K-H, Hellwege AM (eds) Landolt-Börnstein Tables, Group III, vol 11. Springer, erlin
Henkelman G, Uberuaga BP, Jónsson H (2000) J Chem Phys 113:9901
Hirth JP, Lothe J (1982) Theory of dislocations, 2nd edn. Wiley, New York
Joós B, Duesbery MS (1997) Phys Rev Lett 78:266
Kresse G, Furthmuller J (1996) Phys Rev B 54:11169
Kresse G, Hafner J (1993) Phys Rev B 47:558
Lehto N, Öberg S (1998) Phys Rev Lett 80:5568
Li J (2003) Model Simul Mater Sci Eng 11:173
Liu XY, Adams JB, Ercolessi F, Moriarty JA (1996) Model Simul Mater Sci Eng 4:293
Lu G, Kioussis N, Bulatov VV, Kaxiras E (2000) Phys Rev B 62:3309
Mishin Y, Farkas D, Mehl MJ, Papaconstantopoulos DA (1999) Phys Rev B 59:3393
Mishin Y, Mehl MJ, Papaconstantopoulos DA (2005) Acta Mater 53:4029
Mishin Y, Mehl JJ, Papaconstantopoulos DA, Voter AF, Kress JD (2001) Phys Rev B 63:224106
Monkhorst HJ, Pack JD (1976) Phys Rev B 13:5188
Mura T (1964) Proc Roy Soc A 280:528
Murr L (1975) Interfacial phenomena in metals and alloys. Addison-Wesley, India
Nabarro FRN (1947) Proc Phys Soc 59:256
Orowan E (1934) Z. Physik 89:605
Peierls R (1940) Proc Phys Soc 52:34
Perdew JP et al (1992) Phys Rev B 46:6671
Polanyi M (1934) Z. Physik 89:660
Sun DY, Mendelev MI, Becker CA, Kudin K, Haxhimali T, Asta M, Hoyt JJ, Karma A, Srolovitz DJ (2006) Phys Rev B 73:024116
Taylor GI (1934) Proc Roy Soc A 362
Tsuru T (2017) Bull Jpn Inst Metals Materia 56:5 (in Japanese)
Tsuru T, Chrzan DC (2015) Sci Rep 5:8793

Tsuru T, Udagawa Y, Yamaguchi M, Itakura M, Kaburaki H, Kaji Y (2013) J Phys: Condens Matter 25:022202
Vítek V (1966) Phys Status Sol 18:687
Vítek V (1968) Philos Mag 18:773
Vitek V (1974) Cryst Latt Def 5:1
Vitek V, Perrin RC, Bowen DK (1970) Philos Mag 21:1049
Volterra V (1907) Ecol Norm Sup 324:405